The Astrophysical Journal, 966:11 (12pp), 2024 May 1 https://doi.org/10.3847/1538-4357/ad2dfb

Neutrino-driven Outflows and the Elemental Abundance Patterns of Very Metal-poor Stars

A. Psaltis[1,2], M. Jacobi[3], F. Montes[4,5], A. Arcones[3,6], C. J. Hansen[7], and H. Schatz[4,5,8]
[1] Department of Physics, North Carolina State University, Raleigh, NC 27695, USA; psaltis.tha@duke.edu
[2] Triangle Universities Nuclear Laboratory, Duke University, Durham, NC 27710, USA
[3] Institut für Kernphysik, Technische Universität Darmstadt, Schlossgartenstr. 2, Darmstadt 64289, Germany; almudena.arcones@physik.tu-darmstadt.de
[4] Facility for Rare Isotope Beams, East Lansing, MI 48824, USA
[5] Joint Institute for Nuclear Astrophysics - CEE, Michigan State University, East Lansing, MI 48824, USA
[6] GSI Helmholtzzentrum für Schwerionenforschung GmbH, Planckstr. 1, Darmstadt 64291, Germany
[7] Institute for Applied Physics, Goethe University Frankfurt, Max-von-Laue-Str. 12, Frankfurt am Main 60438, Germany
[8] Department of Physics and Astronomy, Michigan State University, 567 Wilson Road, East Lansing, MI 48824, USA
Received 2023 December 19; revised 2024 February 14; accepted 2024 February 23; published 2024 April 22

Abstract

The elemental abundances between strontium and silver ($Z = 38$–47) observed in the atmospheres of very metal-poor stars in the Galaxy may contain the fingerprint of the weak *r*-process and νp-process occurring in early core-collapse supernovae explosions. In this work, we combine various astrophysical conditions based on a steady-state model to cover the richness of the supernova ejecta in terms of entropy, expansion timescale, and electron fraction. The calculated abundances based on different combinations of conditions are compared with stellar observations, with the aim of constraining supernova ejecta conditions. We find that some conditions of the neutrino-driven outflows consistently reproduce the observed abundances of our sample. In addition, from the successful combinations, the neutron-rich trajectories better reproduce the observed abundances of Sr–Zr ($Z = 38$–40), while the proton-rich ones, Mo–Pd ($Z = 42$–47).

Unified Astronomy Thesaurus concepts: Core-collapse supernovae (304); Isotopic abundances (867); Nuclear astrophysics (1129); Nucleosynthesis (1131); Observational astronomy (1145); R-process (1324)

1. Introduction

The origin of elements heavier than iron ($Z = 26$) in the cosmos is one of the most intriguing open questions in nuclear astrophysics. Roughly half of them have traditionally been attributed to the rapid neutron-capture process (*r*-process; Horowitz et al. 2019; Cowan et al. 2021). However, its astrophysical site or sites are still disputed, and it is unclear whether other processes such as the *vp*- or the *i*-process contribute as well. A recently confirmed *r*-process site is the merging of two neutron stars (NSMs), which was detected both via gravitational waves (GW170817; Abbott et al. 2017) as well as by electromagnetic follow-up observations of transient kilonova AT2017gfo (Drout et al. 2017). Despite these successes, due to their rather rare nature and long delay times, NSMs appear to be unable to fully account for the evolution of *r*-process abundances in the Galaxy (see, e.g., Côté et al. 2019; Cavallo et al. 2021; Kobayashi et al. 2023). Other astrophysical sites, such as magnetorotational supernovae (Winteler et al. 2012; Nishimura et al. 2017; Reichert et al. 2021, 2023a), may also produce heavy elements up to the third *r*-process peak and the actinides. Detection of ^{244}Pu and ^{60}Fe in deep-sea crust sediments on Earth suggests a core-collapse supernovae contribution for these specific isotopes. However, NSMs can also account for the production of ^{244}Pu (Wallner et al. 2021; Fields & Wallner 2023; Wang et al. 2023; Wehmeyer et al. 2023).

Moreover, neutrino-driven supernovae may explain observations that indicate an early enrichment of the interstellar medium with elements up to around silver, just before the second *r*-process peak (Arcones & Montes 2011). In this paper, we use these lighter heavy elements between strontium and silver ($Z = 38$–47) to constrain supernova conditions by comparing calculated and observed abundances. Spectroscopic studies of very metal-poor stars show a general robustness not only with their *r*-process abundances but also with the solar *r*-process pattern,[9] especially in the lanthanide region (see, for example, Sneden et al. 2000; Hill et al. 2002; François et al. 2007; Roederer et al. 2014, 2022; Sakari et al. 2018; Cain et al. 2020). This robustness does not extend to the lighter heavy elements, between strontium and silver ($Z = 38$–47), where there is a consistent scatter (see, for example, Figures 11 and 7 from Sneden et al. 2008 and Mashonkina et al. 2010, respectively). Moreover, there are some stars with high abundances of lighter heavy elements relative to heavy *r*-process elements between the second and third *r*-process peaks. These stars have a high ratio of *r*-process Sr/Eu (see, in Table 2, the so-called Honda star, HD 122563) compared to the solar *r*-process—$\log \epsilon\,(\mathrm{Sr/Eu}) = 1.46$ (Sneden et al. 2008). Here, we assume that this enhancement may be due to a nucleosynthesis contribution different from the main *r*-process, which is responsible for abundances up to the third *r*-process peak. This additional contribution has been thoroughly discussed in the literature (Wasserburg et al. 1996; Qian & Wasserburg 2000, 2007; Truran et al. 2002; Aoki et al. 2005; Otsuki et al. 2006; Montes et al. 2007; Bisterzo et al. 2014; Hansen et al. 2014; Cristallo et al. 2015, for some notable examples) and operates very early in Galactic evolution.

[9] Solar *r*-process abundances are calculated by subtracting the *s*- and *p*-process contributions from the total abundance pattern (Goriely 1999; Sneden et al. 2008). Recently, Prantzos et al. (2020) proposed a novel approach by using Galactic Chemical Evolution (GCE) models.

Possible candidates include the weak *r*-process (also known as α-process; Woosley & Hoffman 1992; Witti et al. 1994; Qian & Woosley 1996; Hoffman et al. 1997; Wanajo et al. 2001; Arcones & Montes 2011; Wanajo 2013; Hansen et al. 2014; Bliss et al. 2017, 2018) and the νp-process (Fröhlich et al. 2006; Pruet et al. 2006; Wanajo 2006; Wanajo et al. 2011; Nishimura et al. 2019), both occurring in neutrino-driven outflows of explosive astrophysical environments, such as core-collapse supernovae.

In this work, we survey the astrophysical conditions of the neutrino-driven outflows in supernovae ejecta, both neutron-rich and proton-rich, using an extensive library of thermodynamic trajectories that span the relevant parameter space of astrophysical conditions. We use superpositions of different conditions and compare the resulting nucleosynthesis with observations of very metal-poor stars that show an overproduction of first *r*-process peak isotopes compared to Eu. We aim to pinpoint astrophysical conditions that are favorable to replicating the observed abundances of heavy-element abundances between Sr and Ag in very metal-poor stars.

This paper is structured as follows: in Section 2, we present the astrophysical conditions we used in the present study. In Section 3, we discuss the very metal-poor star sample we use to compare our nucleosynthesis calculations to. In Section 4, we present our procedure to compare observations with combinations of astrophysical conditions, and in Section 5, we show our results. Finally, in Section 6, we present our conclusions and a discussion.

2. Astrophysical Conditions

In this section, we discuss the astrophysical conditions used in our analysis and focus on the distinct nucleosynthesis processes that occur in neutrino-driven outflows: the weak *r*- and the νp-process (see Arcones & Thielemann 2013, and references therein).

Both nucleosynthesis processes start from very hot material ($T > 10$ GK) ejected by neutrinos. This material is composed of dissociated nucleons (see Figure 1 of Psaltis et al. 2022a, for a schematic). Depending on the electron–neutrino and electron–antineutrino energies and luminosities, and on how fast the matter expands, the ejected material can be neutron- or proton-rich. Core-collapse supernovae are complex and asymmetric, and conditions evolve rapidly with time. Therefore, their ejecta are a mixture of materials that encounter different types of conditions. Current simulations show that neutrinos drive most of the matter to proton-rich conditions. However, some bubbles or pockets of material expand quickly and stay slightly neutron-rich (for example, O'Connor 2015; Harris et al. 2017; Müller et al. 2017; Eichler et al. 2018; Wanajo et al. 2018; Bollig et al. 2021; Burrows & Vartanyan 2021; Bruenn et al. 2023; Navó et al. 2023).

The nucleosynthesis of neutrino-driven outflows can be determined from thermodynamic trajectories, characterized by their expansion timescale (τ), entropy (s), and electron fraction (Y_e; see Qian & Woosley 1996; Arcones & Bliss 2014). Each trajectory provides the time evolution of temperature and density, as well as neutrino energies and luminosities, which are used to calculate the associated nucleosynthesis with a nuclear reaction network. According to the electron fraction Y_e, nucleosynthesis can be the weak *r*- ($Y_e < 0.5$) or the νp-process ($Y_e > 0.5$). In previous works, we focused on individual conditions by analyzing single trajectories (Arcones & Montes 2011; Bliss et al. 2018; Psaltis et al. 2022). To account for the diversity of conditions in supernovae, in this work we explore a total of 50 conditions, either neutron-rich or proton-rich, to explain the $Z = 38$–47 abundance pattern of Galactic metal-poor stars. In Figure 1, we present those trajectories in the eentropy per baryon/expansion timescale/Y_e phase space at around 10 GK (when we start the associated nucleosynthesis using a nuclear reaction network): the 36 neutron-rich trajectories used in this study are the same as in Bliss et al. (2020). The trajectories were produced within a spherical steady-state wind model (Bliss et al. 2018), therefore they cannot account for non-monotonic evolution. This may have an impact on the amount of matter ejected with a given pattern (Sieverding et al. 2023), or even on the production of some elements by the νp-process (Arcones et al. 2012). A non-monotonic evolution may change the parameters (Y_e, entropy per baryon, and expansion timescale) that are directly linked to a pattern. Future simulations will show how much matter is ejected in trajectories following a homologous expansion and how much is affected by non-monotonic behavior.

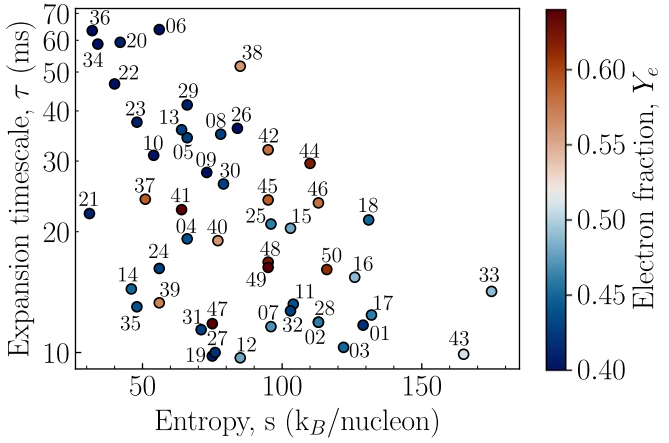

Figure 1. Astrophysical conditions in the entropy per baryon s and expansion timescale τ space. The color code corresponds to the electron fraction Y_e.

2.1. *Weak* r*-process*

In moderate neutron-rich outflows, as the ejecta expand and cool down, mainly iron-peak nuclei are produced via the nuclear statistical equilibrium (NSE). The main reaction channel that links the nucleosynthesis from $A < 5$ nuclei across the $A = 5$ and $A = 8$ stability gaps to the CNO element region and beyond is $\alpha + \alpha + n \rightarrow {}^{9}\mathrm{Be}$, followed by the ${}^{9}\mathrm{Be}(\alpha, n){}^{12}\mathrm{C}$. At $T \approx 5$ GK, NSE cannot be maintained anymore and an α-rich freeze-out occurs. Nucleosynthesis proceeds mainly through charged-particle reactions, (α, n), (p, n), and (α, γ), as well as neutron captures, (n, γ). When the temperature falls to $\approx$1.5–3 GK, the α-induced reactions become too slow and the nucleosynthesis of heavier nuclei ceases. This scenario is known as the weak *r*-process or α-process (Woosley & Hoffman 1992; Hoffman et al. 1997; Arcones & Montes 2011).

Bliss et al. (2018) explored the relevant parameter space for conditions in the weak *r*-process (Y_e, entropy per baryon, and the expansion timescale) using a steady-state model following Otsuki et al. (2000). Subsequent sensitivity studies by Bliss et al. (2020) and Psaltis et al. (2022) tested the importance of (α, n) reaction rates in the final abundance patterns based on 36 representative trajectories from the CPR2 group[10]—the conditions that produce elements with $Z = 38$–47. These reactions were found to be the main nuclear physics uncertainty in weak *r*-process

[10] The representative trajectories can be found in Bliss (2020).

nucleosynthesis calculations (Bliss et al. 2017, 2020). Psaltis et al. (2022) went a step further and explored the impact of nuclear physics uncertainties on predictions of elemental abundance ratios and compared them with observations of Galactic metal-poor stars. Both studies have motivated several experimental studies in the nuclear astrophysics community (Kiss et al. 2021; Szegedi et al. 2021; Angus et al. 2023, for example).

2.2. νp-process

The *νp*-process operates in proton-rich outflows ($Y_e > 0.5$) and can create lighter heavy elements up to Ag (Fröhlich et al. 2006; Pruet et al. 2006; Wanajo 2006). Furthermore, the *νp*-process can be a mechanism for the production of the lighter *p*-nuclei (Arcones & Montes 2011; Wanajo et al. 2011; Rauscher et al. 2013).

The most abundant isotope during the *νp*-process is ^{56}Ni, which is already reached during NSE by a series of α and p captures starting with the triple α reaction, $\alpha(2\alpha, \gamma)^{12}$C. After the matter drops out of NSE, the abundance distribution is mainly determined by a (p, γ)–(γ, p) equilibrium, due to the large abundance of free protons. Matter gets accumulated in bottlenecks, mainly ^{56}Ni and ^{64}Ge, due to their long β-decay lifetimes. However, electron–antineutrino captures on free protons produce enough neutrons to overcome the bottlenecks via (n, p) reactions (Fröhlich et al. 2006; Pruet et al. 2006; Wanajo 2006). Therefore, the production of elements beyond iron by the *νp*-process depends on the flux of antineutrinos and the abundance of free protons. The efficiency of the process is given by the ratio between free neutrons generated by electron–antineutrino absorption on protons and seed nuclei (Pruet et al. 2006):

$$\Delta_n = \frac{Y_p}{Y_{\rm seed}} \int_{T_9<3} \lambda_{\bar{\nu}_e}\, dt, \tag{1}$$

where Y_p and $Y_{\rm seed}$ represent the proton and seed nuclei abundances, respectively, and $\lambda_{\bar{\nu}_e}$ denotes the rate of antineutrino captures on free protons ($\lambda_{\bar{\nu}} \propto L_{\bar{\nu}} \langle \varepsilon_{\bar{\nu}} \rangle / r^2$, where $L_{\bar{\nu}}$ is the electron–antineutrino energy luminosity, $\langle \varepsilon_{\bar{\nu}_e} \rangle$ their average energy, and r the radius. The efficiency of the *νp*-process and thus Δ_n increases for larger $Y_p/Y_{\rm seed}$ and higher antineutrino energies and luminosities. The proton-to-seed ratio is larger for higher entropies and electron fractions. Typical values of Δ_n for ejecta with $Y_e \lesssim 0.65$ range from 1 to 100.

The astrophysical and nuclear physics uncertainties of the *νp*-process have been explored extensively by Wanajo et al. (2011), Arcones et al. (2012), and Nishimura et al. (2019), and these uncertainties have motivated new measurements of nuclear masses and thermonuclear reaction rates (e.g., Fallis et al. 2011; Xing et al. 2018; Randhawa et al. 2021; Psaltis et al. 2022b).

Similarly to Bliss et al. (2018), we calculate neutrino-driven wind trajectories for proton-rich conditions. We vary the electron fraction at $T = 10$ GK between 0.51 and 0.65 and assume that the number luminosities are the same for electron neutrinos and antineutrinos. We use constant antineutrino energy luminosity $L_{\bar{\nu}_e} = 3 \times 10^{51}$ erg s^{-1} and antineutrino energy $\langle \varepsilon_{\bar{\nu}_e} \rangle = 16.66$ MeV. We should note that increasing the average energy or number luminosity of antineutrinos while keeping the electron fraction constant increases Δ_n and thus leads to the formation of heavier nuclei. However, the effect is almost equivalent to changing Δ_n by other means (e.g., by increasing the entropy or electron fraction). It is thus sufficient for our purpose to only consider one value for the antineutrino luminosity and average energy.

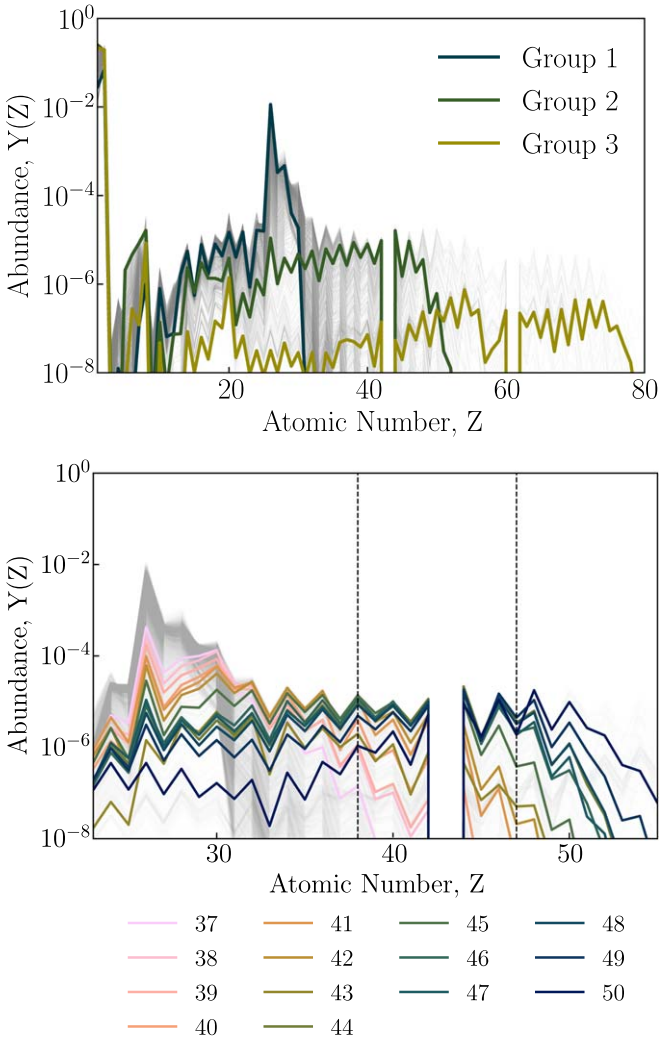

Figure 2. (Top) Abundance patterns for the proton-rich trajectories ($Y_e > 0.5$). A representative pattern for each of the three groups mentioned in the text is shown in color. (Bottom) Abundance patterns for the 14 trajectories used in the present study. The strontium–silver ($Z = 38$–47) region is indicated by the dashed vertical lines.

Figure 2 shows the abundance patterns of all the $Y_e > 0.5$ trajectories. These patterns can be sorted into three groups: mainly iron-peak nuclei without any significant production of $Z > 30$ elements, patterns showing production of elements between strontium and silver, and patterns that can produce elements up to around $Z = 80$. The second group, from which we selected fourteen representative trajectories (37–50 in Table 1, and shown in the lower panel of Figure 2), produces elements between strontium and silver. The trajectories responsible for the third group (with abundances up to around $Z = 80$) are too extreme and are probably rarely or never found in ccSNe explosions. The proton-rich trajectories have a smaller variability in the final abundance pattern than the neutron-rich ones. The reaction flow of the *νp*-process is much more constrained compared to the weak *r*-process, which operates on the neutron-rich side of the stability valley (Arcones & Montes 2011). For this reason, in Table 1 we select only 14 proton-rich conditions, compared to 36 neutron-rich conditions.

Table 1
Main Astrophysical Conditions for the Trajectories Used in the Present Study

Trajectory	Y_e	s (k_B/nucleon)	τ (ms)	Δ_n
01	0.42	129	11.7	⋯
02	0.45	113	11.9	⋯
03	0.45	122	10.3	⋯
04	0.44	66	19.2	⋯
05	0.43	66	34.3	⋯
06	0.40	56	63.8	⋯
07	0.47	96	11.6	⋯
08	0.43	78	35.0	⋯
09	0.40	73	28.1	⋯
10	0.40	54	31.0	⋯
11	0.44	104	13.2	⋯
12	0.48	85	9.7	⋯
13	0.43	64	35.9	⋯
14	0.45	46	14.4	⋯
15	0.48	103	20.4	⋯
16	0.49	126	15.4	⋯
17	0.46	132	12.4	⋯
18	0.45	131	21.4	⋯
19	0.41	75	9.8	⋯
20	0.41	42	59.3	⋯
21	0.41	31	22.2	⋯
22	0.40	40	46.7	⋯
23	0.41	48	37.5	⋯
24	0.43	56	16.2	⋯
25	0.46	96	20.9	⋯
26	0.40	84	36.2	⋯
27	0.42	76	10.0	⋯
28	0.46	113	11.9	⋯
29	0.41	66	41.4	⋯
30	0.43	79	26.3	⋯
31	0.43	71	11.4	⋯
32	0.43	103	12.7	⋯
33	0.49	175	14.2	⋯
34	0.40	34	58.7	⋯
35	0.44	48	13.0	⋯
36	0.40	32	63.4	⋯
37	0.59	51	24.1	3.4
38	0.56	85	51.7	5.5
39	0.57	56	13.3	5.9
40	0.56	77	19.0	8.8
41	0.64	64	22.7	11.0
42	0.58	95	32.0	14.8
43	0.51	165	9.9	16.8
44	0.62	110	29.6	35.3
45	0.59	95	24.0	21.6
46	0.58	113	23.6	31.1
47	0.64	75	11.8	32.1
48	0.62	95	16.8	34.6
49	0.64	95	16.3	44.2
50	0.61	116	16.1	57.4

Note. Δ_n is defined only for trajectories with $Y_e > 0.5$ (νp-process).

3. Abundance Observations from Metal-poor Stars

Figure 3 and Table 2 present the stellar abundance observations[11] used to compare to our nucleosynthesis calculations. These very metal-poor stars ([Fe/H] < -2) show high abundances of the light neutron-capture elements relative to heavy r-process elements between the second and third r-process peaks, as evidenced by their high ratio of Sr/Eu. The abundances in Figure 3 are normalized to the solar r-process strontium. There is a ≈0.5 dex difference compared to the respective solar r-process abundances (bottom panel, Figure 2). The stars selected for this work are a subset of the star sample in Psaltis et al. (2022), ensuring that the stars have as many observed elements in the $Z = 38$–47 region as possible. For elements such as niobium and silver, there are not many published observations in the literature, compared to strontium–yttrium–zirconium, and that poses a challenge when comparing our nucleosynthesis theories to observations. Part of the reason for this lack of data is related to the wavelength of the strongest transitions of the heavy elements. Elements like silver and palladium show their strongest absorption lines in the near-UV/blue part of the spectrum (<350 nm; Hansen et al. 2012), which is very hard to analyze, due to line blending, and many spectrographs do not even cover this range, due to low throughput of the signal. In Figure 3, technetium (Tc) is missing. The reason for this is that Tc is radioactive with a lifetime that is many orders of magnitude shorter than the age of the weak r-process event that created the abundance pattern. For comparison, while Sr shows much intrinsic stronger lines (for example at 407.7 nm), Y and Zr show features in the visible spectrum around 500 nm, which is covered by most large surveys. The two stars with the most observed abundances in the Sr–Ag range in our sample are HD 122563 and HD 88609 (Honda et al. 2007).

Observational uncertainties in abundances can be either statistical (random) or systematic. The first type originates mainly from line-to-line dispersion that can be caused by signal-to-noise ratio, uncertainties in line measurements or continuum placement,

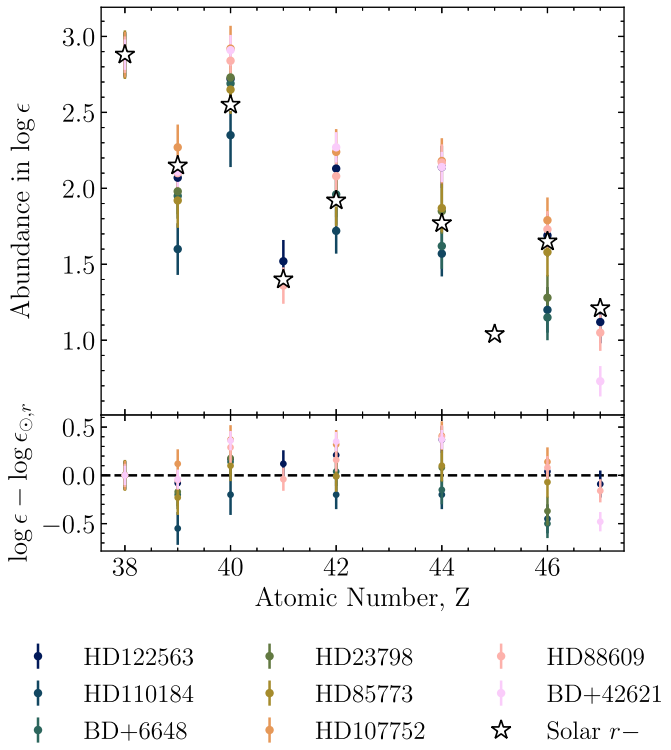

Figure 3. Elemental abundances of the stellar sample used in this study *normalized* to the solar r-process strontium ($Z = 38$) (Lodders et al. 2009). The difference from the solar r-process residuals is shown in the bottom panel. The error bars show *statistical* (random) errors.

[11] Abundances are shown in $\log \epsilon_X = \log\left(\frac{N_X}{N_H}\right) + 12$.

Table 2
Observations of Metal-poor Stars Used in the Present Work, in Units of $\log \epsilon$

Star	Sr	Y	Zr	Nb	Mo	Ru	Pd	Ag	Sr/Eu	Sr/Fe	[Fe/H]
BD+42_621	0.21(10)	–0.56(10)	0.24(10)	⋯	–0.40(10)	–0.53(10)	⋯	–1.94(10)	1.64	–4.75	–2.48
BD+06_648	0.95(15)	0.02(15)	0.76(15)	⋯	0.03(15)	–0.31(15)	–0.78(15)	⋯	2.33	–4.38	–2.11
HD 23798	0.86(15)	–0.04(15)	0.71(18)	⋯	–0.11(15)	–0.17(15)	–0.74(15)	⋯	2.36	–4.32	–2.26
HD 85773	0.00(16)	–0.96(18)	–0.23(16)	⋯	–0.97(16)	–1.01(16)	–1.30(16)	⋯	2.08	–4.82	–2.62
HD 88609	–0.20(12)	–0.98(10)	–0.24(16)	–1.72(12)	–1.00(12)	–0.91(12)	–1.35(12)	–2.03(12)	2.69	–4.62	–2.87
HD 107752	–0.26(15)	–0.87(15)	–0.22(15)	⋯	–0.90(15)	–0.96(15)	–1.35(15)	⋯	1.76	–4.85	–2.85
HD 110184	0.46(15)	–0.82(17)	–0.07(21)	⋯	–0.70(15)	–0.85(15)	–1.22(15)	⋯	2.49	–4.46	–2.52
HD 122563	–0.12(14)	–0.93(9)	–0.28(16)	–1.48(14)	–0.87(14)	–0.86(14)	–1.31(14)	–1.88(14)	2.65	–4.84	–2.72

Notes. The abundance data were taken by Hansen et al. (2012, 2014; BD+42_621); Aoki et al. (2017; BD+06_648, HD 23798, HD 85773, HD 107752, and HD 110184); Honda et al. (2007) and Hansen et al. (2014; HD 88609); and Honda et al. (2007; HD 122563). The metallicities [Fe/H] are listed using the spectroscopic notation $[\mathrm{Fe/H}] = \log \epsilon_{Fe,\star} - \log \epsilon_{Fe,\odot}$. The uncertainties listed for Sr–Ag are *statistical* (random).

cosmic-ray or sky-line contamination, atomic data uncertainties, and other factors. Systematic errors are related to the atmospheric parameters used to determine the abundances ($T_{\rm eff}$, $\log g$, microturbulent velocities, and metallicities) and the use of LTE or non-LTE (1D or multi-D) Amarsi et al. (2016). In Table 2, we report only the *random* uncertainties, which we will use when fitting the abundance patterns in Section 4.

4. Methods

We performed nucleosynthesis calculations using the `WinNet` reaction code (Winteler et al. 2012; Reichert et al. 2023b) and the same setup as in Psaltis et al. (2022), with the default reaction rates from the JINA Reaclib (Cyburt et al. 2010) database and the (α, xn) reaction rates from Mohr et al. (2021), for the astrophysical conditions of Table 1.

In the following, we discuss our approach to match the astronomical observations using our extended library of astrophysical conditions (see Section 2). Linear combinations of the different trajectories for the predicted abundance distribution were created using

$$P = \sum_{i=1}^{r} w_i Y_i, \tag{2}$$

where the multiplication factors $w_i > 0$ represent the scaling applied to the abundance distribution Y_i, while r is a free parameter indicating the number of distinct trajectories (conditions) selected for each combination from the sets presented in Table 1. As we shall show in the following, combinations with $r < 4$ are sufficient to match observations. The number of unique combinations of N trajectories taken r at a time is $C_r = N!/r!(N-r)!$, that is, for 2 and 3 selections out of the 50 trajectories in Table 1, there are 1225 and 19,600 unique combinations, respectively. Each predicted abundance pattern P is compared to the observed abundance pattern O of the metal-poor stars in Table 2. Finding the weights that best fit the observational pattern for each combination is a linear regression (or least-squares) problem. To solve it, we need to

$$\text{minimize } ||Aw - O||^2, \tag{3}$$

where A is a $k \times r$ matrix containing the r individual abundance patterns Y_i of the combination for k elements, w is the coefficient array (of length r), and O is the observation pattern (of length k):

$$A = \begin{bmatrix} Y_{11} & \cdots & Y_{1k} \\ \vdots & \ddots & \vdots \\ Y_{r1} & \cdots & Y_{rk} \end{bmatrix}, \; w = \begin{bmatrix} w_1 \\ \vdots \\ w_N \end{bmatrix}.$$

The coefficients w_i self-normalize the predictions to the observations. We can define the relative contribution of each trajectory in the combination F_i as follows:

$$F_i = \frac{w_i}{\sum_{i=1}^{r} w_i}. \tag{4}$$

This way, we can examine the most common thermodynamical properties (Y_e, entropy per baryon, and expansion timescale) that reproduce the elemental abundances in our star sample, and compare them with hydrodynamical simulations (see Section 5).

To solve the linear regression problem, we used the `scikit-learn` (Buitinck et al. 2013) package and weighted the sample according to the *statistical (random)* observational uncertainty (Table 2).

The goodness of each fit to the observational data was assessed using a reduced χ^2_ν:

$$\chi^2_\nu = \frac{1}{\nu} \sum_{i=1}^{k} \left(\frac{O(i) - P(i)}{\sigma(O(i))} \right)^2, \tag{5}$$

where $\sigma(O(i))$ is the observational *statistical* uncertainty of element i, as shown in Table 2, and $\nu = k - r$ are the degrees of freedom. In general, a lower χ^2_ν value indicates a better model fit to the data, and values close to unity, assuming a reasonable number of data points, likely exhibit acceptable variance. Nevertheless, we are only fitting 6–8 points for each star, and each observational measurement has an inherent uncertainty $\sigma(O(i))$. To address these issues, we employed a Monte Carlo resampling technique by generating 10^4 resampled data sets, according to the observational uncertainty of each star (Table 2). For each of these data sets, we recalculated the reduced χ^2_ν value using Equation (5). This approach effectively simulates the impact of random errors and variability in the data. The result was a distribution of χ^2_ν values, representing the range of fits we could expect due to data uncertainties. In the following, we shall report the median value of the resulted distributions, $\chi^2_{\nu,0.5}$.

Following the discussion in Andrae et al. (2010), the χ^2_ν metric can only be used effectively for the true model having the true parameter values with a priori known measurement

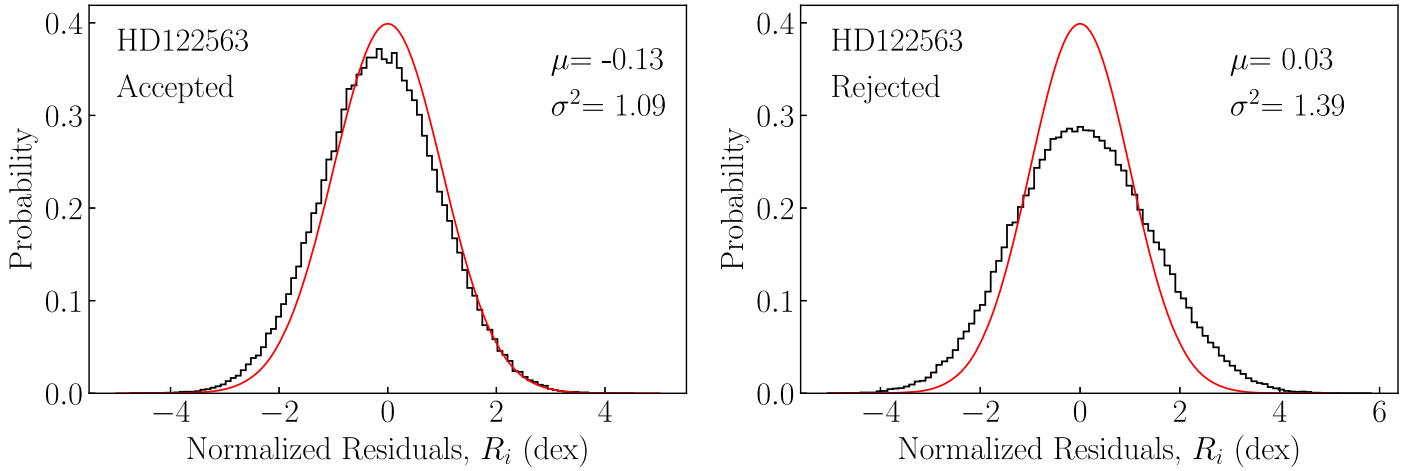

Figure 4. Distribution of normalized residuals for star HD 122563 using two trajectories ($r = 2$). The red line shows the normal distribution with $\mu = 0$ and $\sigma^2 = 1$. The left panel shows an accepted fit, while the right shows a rejected one.

errors. In that case, the normalized residuals,

$$R_i = \frac{O(i) - P(i)}{\sigma(O(i))}, \tag{6}$$

are normally distributed with mean $\mu = 0$ and variance $\sigma^2 = 1$ ($R_i \sim$ N(0, 1), where N denotes the normal (i.e., Gaussian) probability density and "$\sim$" stands for "follows this distribution"). To accept a model according to that analysis, we performed an Anderson–Darling test (AD test) (Scholz & Stephens 1987) to the normalized residuals R_i of each star and accepted those that followed $\sim$N(0, 1) at the 5% significance level. In Figure 4, we show an example for an accepted and a rejected fit for star HD 122563 (for a full list of the accepted combinations, please see Tables 3 and 5).

5. Results

In this section, we present our results for the different combinations of astrophysical conditions: neutron-rich, proton-rich, and mixtures of both. For each star, we shall report successful fits using the lowest number of trajectories r necessary to obtain them.

5.1. Neutron-rich Conditions, $Y_e < 0.5$

The best combinations of two or three neutron-rich conditions (trajectories 1–36 from Table 1, $r = 2,3$) that fit the elemental abundances are shown in Table 3. We note that, as already mentioned in the preceding discussion, we are looking for *acceptable* fits. Figure 5 (top) shows a sample case of an accepted fit using two neutron-rich conditions ($r = 2$) for metal-poor star BD+06_648 using observational data from Aoki et al. (2017). Only two components seem to reproduce the observations, one for the $Z = 38$–42 region and the other for the $Z = 44$–47 abundances (Figure 5, middle). Such behavior is typical for our fits.

Of all the metal-poor stars considered in Table 2, only stars HD 88609 and HD 122563 cannot provide acceptable fits for $r = 2$, 3. This discrepancy is likely attributable to their comparatively higher number of measured elemental abundances (8), which appears to adversely impact the fitting

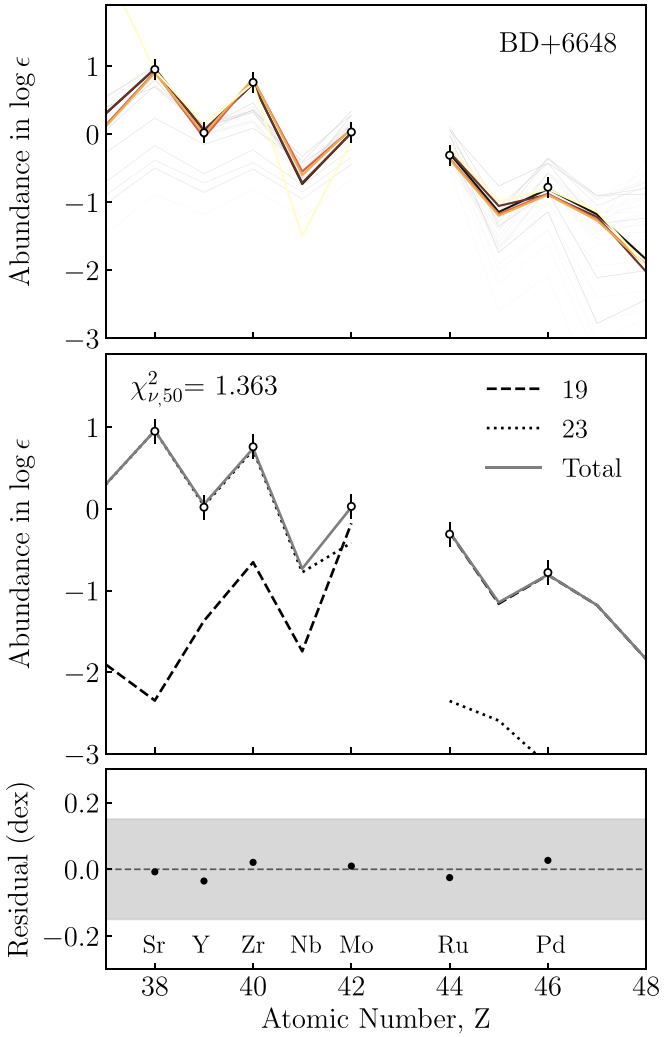

Figure 5. (Top) Fits for BD+06_648 abundances using two neutron-rich conditions. Five colored lines represent accepted fits. Gray lines represent all 630 of the unique combinations of two neutron-rich conditions from Table 1 using the best weights w_i. (Middle) Decomposition of the best fit ($\chi^2_{\nu,50}$ = 1.363) for BD+06_648 using two neutron-rich conditions. (Bottom) Residuals of the best fit. The band shows the maximum random uncertainty of this star. See the text for details.

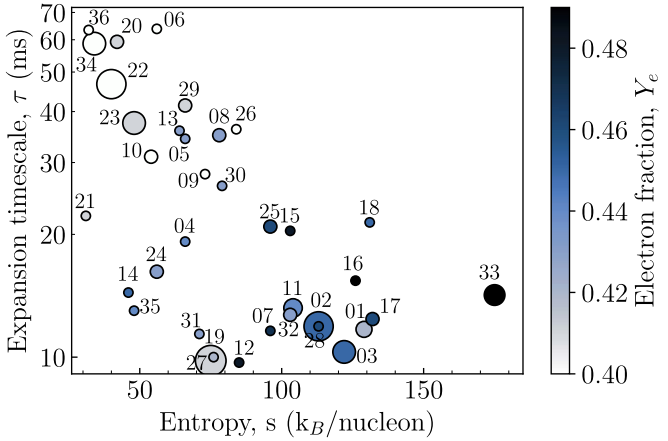

Figure 6. Same as Figure 1, but showing only neutron-rich conditions. The size of each point is proportional to the number of times it appears in accepted fits when combining only neutron-rich conditions.

accuracy compared to other stars. For stars HD 23798 and BD +06_648, we find acceptable fits for $r = 2$. The rest of the stars require $r = 3$ fits to be considered acceptable (see Table 3). In general, neutron-rich trajectories are able to reproduce well the observational Sr–Zr abundances, but they show some discrepancy in the Ru–Ag region. The most extreme example is HD 110184, which has the highest Sr/Ru and Sr/Mo ratios between all the stars in our sample and requires at least three components to obtain an acceptable fit.

The neutron-rich trajectories that appear in the $r = 2$ and $r = 3$ accepted fits are shown in Figure 6 in the relevant phase space. We find two clusters of conditions that are the most favorable in neutrino-driven ejecta: mainly $0.42 < Y_e < 0.45$, high entropy ($s > 80\,k_B$/nucleon), and short expansion timescale ($\tau < 15$ ms), and a smaller cluster with low $Y_e \approx 0.40$, low entropy ($s < 40\,k_B$/nucleon), and high expansion timescale ($\tau > 40$ ms).

5.2. Proton-rich Conditions, $Y_e > 0.5$

As we did with the neutron-rich conditions, we also performed calculations using combinations of two and three trajectories for the proton-rich conditions ($r = 2$, 3). The nucleosynthesis path of the νp-process is more robust compared to that of the weak r-process (Arcones & Montes 2011; Arcones & Bliss 2014; Nishimura et al. 2019). For this reason, we find much less variation in the abundance patterns of the different trajectories. The parameter that is most commonly used to assess the efficiency of the νp-process in producing heavy elements is the number ratio Δ_n (Equation (1)), as we discussed in Section 2. Nishimura et al. (2019) have shown that a $\Delta_n \gtrsim 50$ leads to the production of $A > 120$ nuclei, which we also confirm in our calculations.

None of the two proton-rich combinations produced an acceptable fit, as shown by the large $\chi^2_{\nu,50}$ values in Table 4. The lowest $\chi^2_{\nu,50}$ (for star HD 110184) is 2.482, which is higher than any of the acceptable fits when using only neutron-rich conditions. Nevertheless, in Figure 7, we show the best combination for HD 110184. Trajectories 39 and 43 appear in all stars in Table 4, except in BD+42_621. Interestingly, in the case of HD 107752, only one trajectory (43) produced the lowest $\chi^2_{\nu,50}$. We extended our analysis for $r = 3$ proton-rich trajectories, to investigate whether we can obtain acceptable

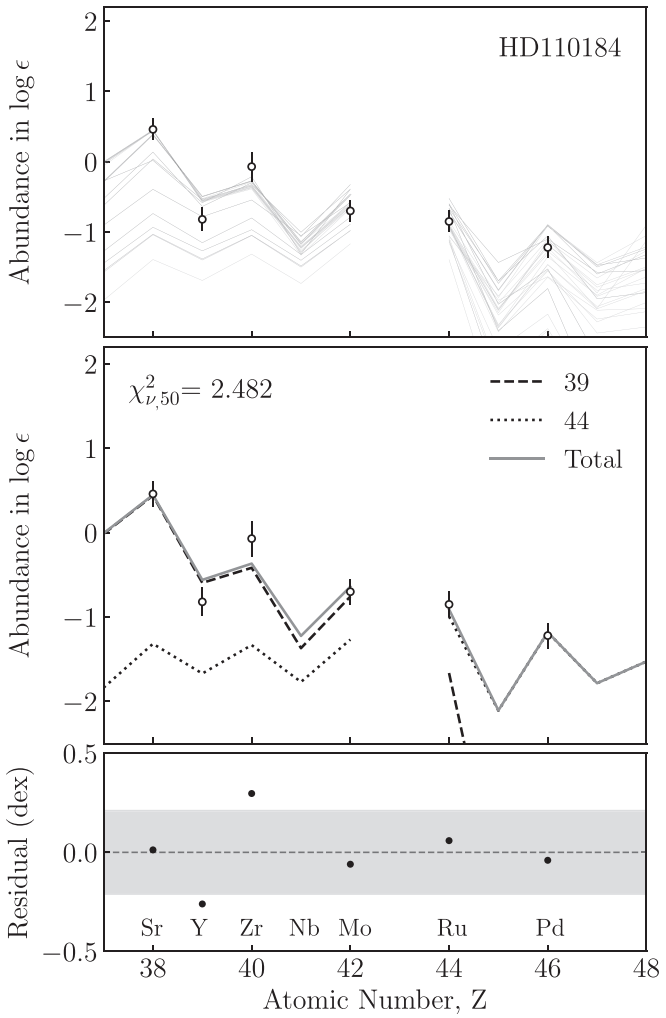

Figure 7. Same as Figure 3, but using two proton-rich trajectories for star HD 110184. See the text for details.

fits. Again, we did not obtain any acceptable fits, and for some stars, such as HD 23798 and HD 107752, we obtained the same results as in $r = 2$, showing that increasing the r value causes the linear regression problem to begin to degenerate.

The inability of the proton-rich trajectories to produce acceptable fits can be explained by the variations in their Sr–Zr triplet abundances (see Figure 2 compared to Figure 3). As we shall discuss in the following, the proton-rich trajectories can reproduce more accurately the Ru–Ag ($Z = 42 - 47$) region of the observed abundance pattern in very metal-poor (VMP) stars.

5.3. Combination of Neutron-rich and Proton-rich Conditions

Sophisticated multidimensional supernova simulations show that neutrino-driven ejecta are very complex and have both neutron- and proton-rich components (Lentz et al. 2015; Janka et al. 2016; Vartanyan et al. 2019; Burrows et al. 2020; Bollig et al. 2021; Sandoval et al. 2021, for some recent examples). For this reason, we decided to combine mixtures of both neutron-rich and proton-rich conditions.

Combining both neutron-rich and proton-rich conditions yields successful fits for all the stars in our sample for $r = 2$, except for HD 110184 and HD 88609, for which we had to

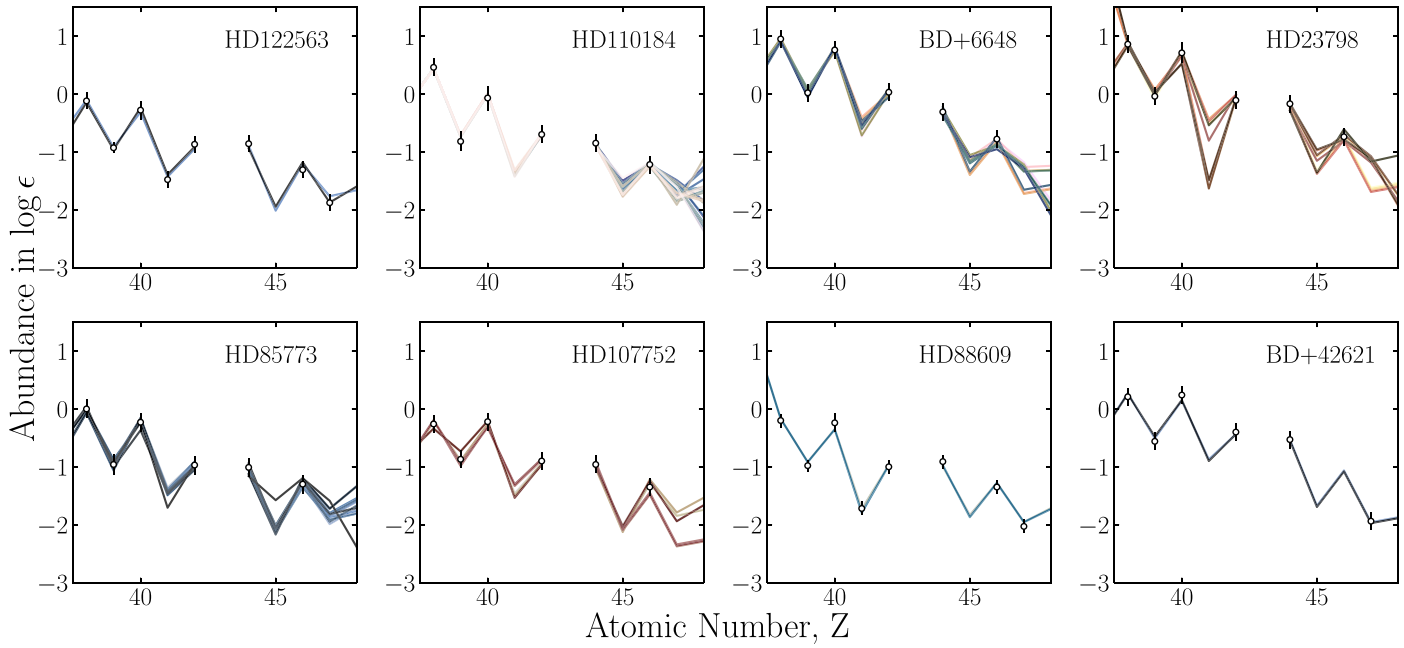

Figure 8. Abundance patterns of the accepted fits using $r = 2$ for the stars in our sample. It should be noted that, for HD 110184 and HD 88609, we use the $r = 3$ accepted fits. See the text for details.

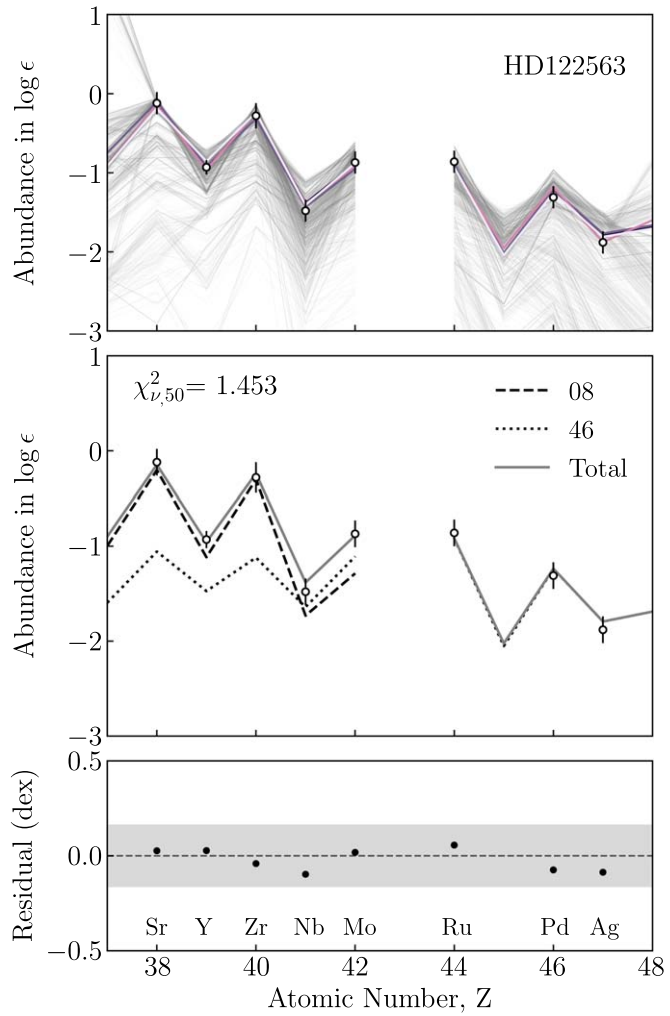

Figure 9. Same as Figure 3, but with the combination of one proton-rich and one neutron-rich condition for the star HD 122563. See the text for details.

extend to $r = 3$ to find successful fits (see Table 5 and the previous discussion). Out of the total 83 successful fits, 61 were mixtures of proton-rich and neutron-rich trajectories, while the rest were neutron-rich-only combinations. In Figure 8, we present the results for all the stars in our sample, using two or three trajectories ($r = 2$, 3; only neutron-rich, only proton-rich, and a mixture of neutron-rich and proton-rich).

In Figure 9, we show an accepted fit for HD 122563. The proton-rich trajectories seem to more successfully reproduce the Ru–Ag ($Z = 44$–47) region. To further examine this, for each accepted fit, we calculate the weighted average $Y_e(Z) = (\sum_{i=1}^{r} w_i Y_i(Z) Y_{e,i})/(Y_{\rm total}(Z))$ for each element in $Z = 38$–47. In Figure 10, we show the residuals of the accepted fits for BD +06_648 for each element, color-coded according to their respective $Y_e(Z)$. Sr–Zr is better produced by mean $Y_{\rm e} =$ 0.43–0.45. Mo requires a combinations of proton-rich and neutron-rich material, which yields a mean $Y_e = 0.50$. Finally, Ru and Pd need proton-rich conditions with a mean $Y_e = 0.51$ and 0.61, respectively. This result is in agreement with Aoki et al. (2017), who argued that the decease observed in the abundances between Mo and Pd can be attributed to the weak *r*-process. The behavior we described is found in all the successful fits, which require one proton-rich and one neutron-rich trajectory, and it can also explain the reason why we were not able to find acceptable fits using only proton-rich trajectories.

In Figure 11, we map these conditions in the relevant phase space to study the topology of the accepted fits under ccSNe conditions. There is a group of trajectories with moderate to high entropy ($40 < s < 113\,k_B$/nucleon) and expansion timescale ($16 < \tau < 60$ ms) that participates in the majority of the accepted fits. A smaller group is located in a region with low expansion timescale ($\tau < 12$ ms) and high entropy ($60 < s < 120\,k_B$/nucleon). An important conclusion here is that the proton-rich trajectories dominate the accepted combinations, having

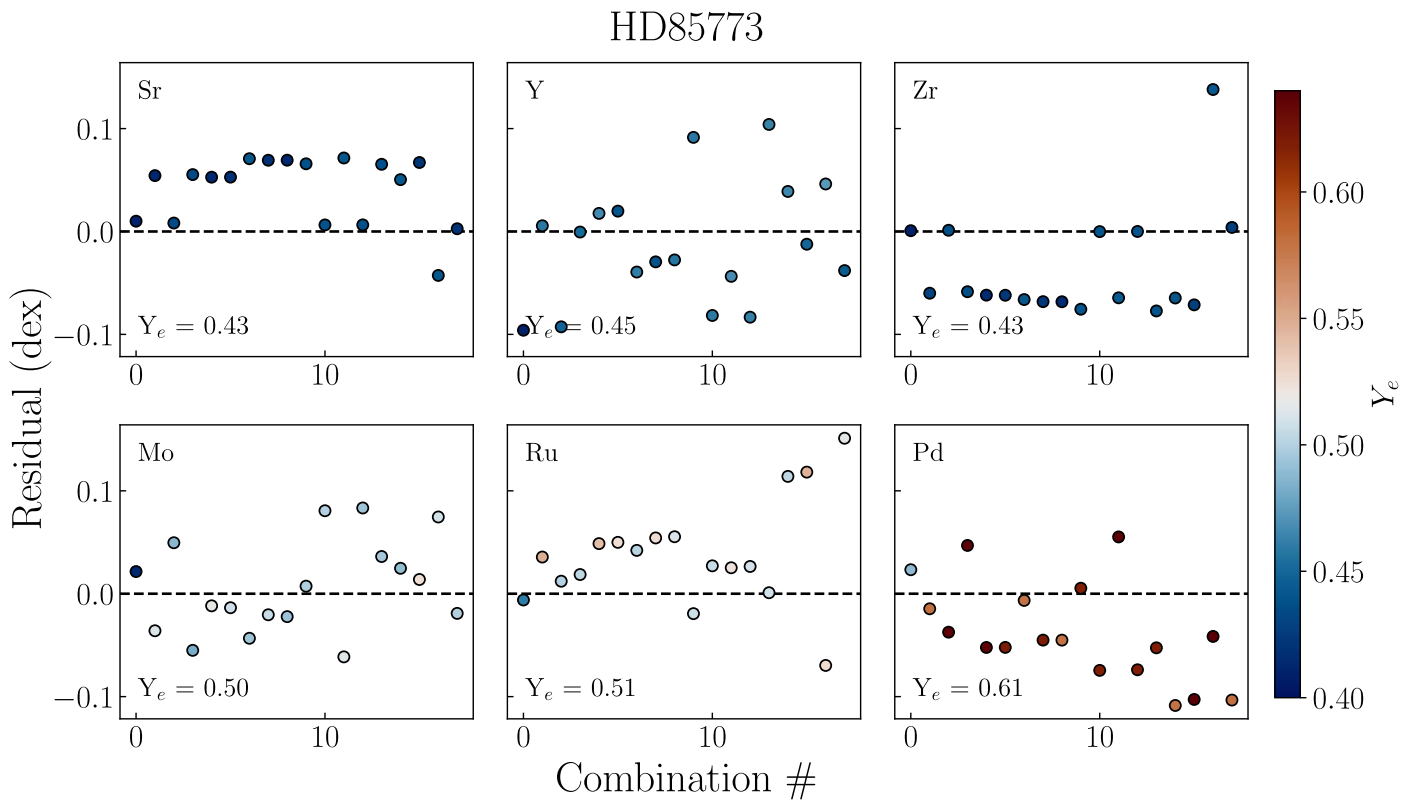

Figure 10. Residuals for the accepted fits (18) for HD 85773. Each panel shows the residuals for a particular element, and the points are color-coded according to the weighted average $Y_e(Z) = (\sum_{i=1}^{r} w_i Y_i(Z) Y_{e,i})/(Y_{\rm total}(Z))$ of the trajectories used for that element. It is evident that elements Sr, Y, and Zr are better fitted using neutron-rich conditions. Mo needs a combination of neutron-rich and proton-rich material. Ru and Pd are best fitted using proton-rich conditions. See the text for details.

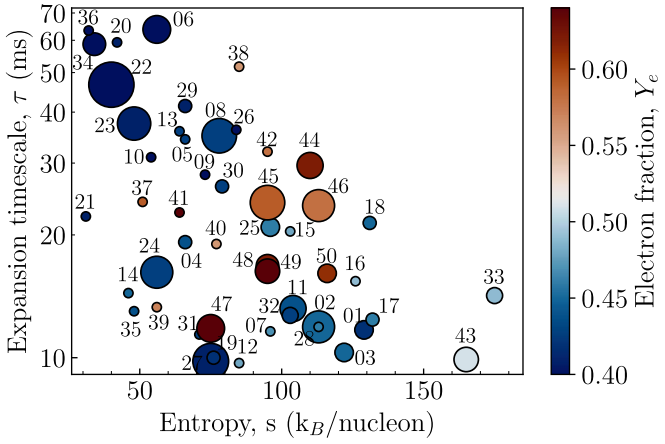

Figure 11. Same as Figure 1. The size of each point is proportional to its number of appearances in the accepted fits shown in Table 5.

much larger R_i values (Equation (4)) compared to those of the neutron-rich counterparts (see Table 5 for a detailed list).

6. Conclusions and Discussion

In the context of the present work, we used thermodynamical trajectories of neutrino-driven ejecta from Bliss et al. (2018; neutron-rich) and new proton-rich ones, spanning the relevant phase space (Y_e, s, τ), to fit the abundance patterns of the light neutron-capture elements between strontium and silver. For the first time, we combined both neutron-rich (weak r-process) and proton-rich (νp-process) trajectories. Because ccSN is a complex phenomenon that produces a variety of conditions in its neutrino-driven phase, combining multiple astrophysical conditions allows for a variety of nucleosynthesis processes to occur.

We find that specific conditions are shown in multiple combinations in different stars (detailed lists of which are provided in Tables 3 and 5, and maps in Figures 6 and 11), suggesting that they might be the dominant contributors for the production of $Z = 38$–47 elements in neutrino-driven outflows of ccSNe. Our results are consistent with recent multidimensional simulations, which show that the neutrino-driven ejecta are mainly proton-rich. However, the small neutron-rich component is crucial to reproduce the Sr–Zr abundances.

The analysis we have performed in the present work is based only on the abundances of *elemental* and not *isotopic* abundances. Because it is extremely difficult to discern different isotopes in the atmospheres of metal-poor stars, a viable alternative would be presolar stardust grains of ccSN origin, such as SiC (Pignatari et al. 2013; Liu et al. 2018).

To enhance the robustness of our nucleosynthesis theories, further observations of metal-poor stars within the intriguing range from strontium to silver are essential. Additionally, comprehensive nucleosynthesis yields from multidimensional core-collapse supernova simulations will contribute significantly to advancing our understanding of their production in the Galaxy.

Acknowledgments

This work was supported by the Deutsche Forschungsgemeinschaft (DFG; German Research Foundation)–Project No. 279384907–SFB 1245, the State of Hesse within the Research Cluster ELEMENTS (Project ID 500/10.006), and the National

Science Foundation under grant No. OISE-1927130 (IReNA). A.P is also supported by the U.S. Department of Energy, Office of Science, Office of Nuclear Physics, under Award Number DE-SC0017799 and Contract Nos. DE-FG02-97ER41033 and DE-FG02-97ER41042. The network calculations were performed on the GSI Virgo HPC cluster. F.M. and H.S. are supported by the US National Science Foundation under award numbers PHY-1913554 and PHY 14-30152 (JINA-CEE) and NSF grant No. 2209429. C.J.H. acknowledges the European Union's Horizon 2020 research and innovation program under grant agreement No. 101008324 (ChETEC-INFRA). A.P. would like to thank Richard Longland and Christian Iliadis for fruitful discussions.

Software: `h5py` (Collette 2013), `IPython` (Pérez & Granger 2007), `Jupyter` (Kluyver et al. 2016),`matplotlib` (Hunter 2007), `numpy` (Harris et al. 2020), `pandas` (The pandas development team 2020), Scientific color maps (Crameri 2021), `sklearn` (Pedregosa et al. 2011)

Appendix

Here we present a comprehensive list of the best combinations for $r = 2,3$ for only neutron-rich (Table 3), only proton-rich (Table 4) and both neutron-rich and proton-rich (Table 5) conditions.

Table 3
Best Combinations of Two or Three Neutron-rich Conditions That Fit the Elemental Abundances of Our Star Sample

Star	Trajectories	Relative Contribution, F_i	$\chi^2_{\nu,50}$
BD+06_648	19, 23	0.1165, 0.8835	1.363
BD+06_648	02, 23	0.1999, 0.8001	1.497
BD+06_648	19, 24	0.0908, 0.9092	1.564
BD+06_648	08, 19	0.9184, 0.0816	1.595
BD+06_648	02, 34	0.0036, 0.9964	1.848
HD 23798	19, 34	0.0023, 0.9977	1.485
HD 23798	02, 34	0.0044, 0.9956	1.518
HD 23798	19, 23	0.1358, 0.8642	1.676
HD 23798	02, 23	0.2317, 0.7683	1.808
BD+42_621	11, 29, 34	0.5793, 0.4207, 0.9865	1.203
HD 85773	02, 03, 23	0.4785, 0.5215, 0.6919	1.154
HD 85773	10, 20, 33	0.1287, 0.8713, 0.4845	1.185
HD 85773	02, 33, 34	0.1345, 0.8655, 0.9806	1.189
HD107752	02, 03, 25	0.5914, 0.4086, 0.7829	1.272
HD 110184	02, 03, 22	0.1684, 0.0672, 0.7644	1.918
HD 110184	01, 19, 22	0.0432, 0.1126, 0.8442	1.930
HD 110184	02, 17, 22	0.1354, 0.1162, 0.7484	1.932
HD 110184	19, 22, 33	0.0542, 0.5738, 0.3720	1.946
HD 110184	03, 11, 22	0.0946, 0.1223, 0.7831	1.978
HD 110184	19, 22, 32	0.0908, 0.8587, 0.0505	1.951
HD 110184	03, 19, 22	0.0636, 0.0991, 0.8373	1.959
HD 110184	11, 22, 33	0.0584, 0.5010, 0.4406	1.964
HD88609	19, 23	0.2209, 0.7791	2.678
HD88609	10, 19, 34	0.2902, 0.7098, 0.9951	2.684
HD122563	19, 23	0.2409, 0.7591	2.289
HD122563	10, 19, 36	0.3469, 0.6531, 0.9978	1.982

Notes. The relative contributions F_i and the $\chi^2_{\nu,50}$ are also shown. The combinations below the line are the best but not acceptable fits. See the text for details.

Table 4
Best Combinations of Two and Three Proton-rich Conditions That Fit the Elemental Abundances of Our Star Sample

Star	Trajectories	Relative Contribution, F_i	$\chi^2_{\nu,50}$
HD 122563	39, 43	0.4989, 0.5011	3.157
HD 122563	39, 43, 46	0.5991, 0.3969, 0.0040	2.344
HD 110184	39, 44	0.9981, 0.0019	2.482
HD 110184	39, 44, 46	0.9977, 0.0013, 0.0010	3.232
BD+06_648	39, 43	0.8080, 0.1920	3.340
BD+06_648	39, 43, 49	0.8080, 0.1920, 0.0000	4.427
HD 23798	39, 43	0.7750, 0.2250	3.002
HD 85773	40, 49	0.9869, 0.0131	3.236
HD 85773	39, 43, 49	0.7947, 0.2037, 0.0015	3.826
HD 107752	43	1.0000	2.730
HD 88609	39, 43	0.5111, 0.4889	3.155
HD 88609	39, 43, 50	0.5696, 0.4275, 0.0029	3.446
BD+42_621	41, 49	0.9876, 0.0124	7.254
BD+42_621	40, 41, 46	0.3999, 0.5731, 0.0271	9.332

Notes. The relative contributions F_i and the reduced $\chi^2_{\nu,50}$ are also shown. None of these combinations is an acceptable fit.

Table 5
Best Combinations of Two or Three Neutron-rich and Proton-rich Conditions That Fit the Elemental Abundances of Our Star Sample

Star	Trajectories	Relative Contribution, F_i	$\chi^2_{\nu,50}$
HD 122563	08, 46	0.0302, 0.9698	1.453
HD 122563	23, 46	0.0231, 0.9769	1.490
BD+06_648	06, 43	0.0015, 0.9985	1.374
BD+06_648	24, 45	0.0478, 0.9522	1.395
BD+06_648	08, 45	0.0536, 0.9464	1.436
BD+06_648	24, 43	0.0024, 0.9976	1.484
BD+06_648	19, 24	0.0908, 0.9092	1.569
BD+06_648	08, 43	0.0027, 0.9973	1.563
BD+06_648	06, 45	0.0313, 0.9687	1.581
BD+06_648	23, 45	0.0407, 0.9593	1.583
HD 23798	06, 45	0.0238, 0.9762	1.409
HD 23798	23, 45	0.0294, 0.9706	1.496
HD 23798	24, 45	0.0362, 0.9638	1.492
HD 23798	06, 43	0.0013, 0.9987	1.886
HD 23798	08, 47	0.0796, 0.9204	1.901
HD 23798	08, 44	0.1112, 0.8888	2.111
HD 85773	23, 46	0.0384, 0.9616	1.418
HD 85773	24, 47	0.0475, 0.9525	1.415
HD 85773	23, 47	0.0413, 0.9587	1.429
HD 85773	24, 46	0.0443, 0.9557	1.443
HD 85773	24, 44	0.0648, 0.9352	1.445
HD 85773	24, 48	0.0564, 0.9436	1.447
HD 85773	08, 48	0.0619, 0.9381	1.460
HD 85773	08, 44	0.0710, 0.9290	1.478
HD 85773	08, 47	0.0522, 0.9478	1.453
HD 85773	06, 46	0.0305, 0.9695	1.489
HD 85773	23, 48	0.0492, 0.9508	1.496
HD 85773	08, 46	0.0487, 0.9513	1.504
HD 85773	23, 44	0.0567, 0.9433	1.503
HD 85773	06, 47	0.0330, 0.9670	1.529
HD 85773	24, 49	0.0627, 0.9373	1.613
HD 85773	08, 49	0.0686, 0.9314	1.642
HD 85773	25, 47	0.0914, 0.9086	1.731
HD 85773	23, 49	0.0549, 0.9451	1.775
HD 107752	25, 46	0.0558, 0.9442	1.436
HD 107752	08, 46	0.0293, 0.9707	1.688
HD 107752	08, 45	0.0161, 0.9839	1.700
HD 107752	06, 45	0.0099, 0.9901	1.702
HD 107752	24, 45	0.0140, 0.9860	1.715
HD 107752	29, 43	0.0004, 0.9996	1.870
HD 107752	04, 45	0.0253, 0.9747	1.887

Table 5
(Continued)

Star	Trajectories	Relative Contribution, F_i	$\chi^2_{\nu,50}$
HD 107752	30, 43	0.0006, 0.9994	1.957
BD+42_621	06, 45	0.0115, 0.9885	1.660
BD+42_621	24, 45	0.0165, 0.9835	1.757
HD 110184	11, 22, 49	0.0228, 0.1566, 0.8206	1.895
HD 110184	02, 22, 50	0.0342, 0.1556, 0.8102	1.902
HD 110184	02, 22, 32	0.1546, 0.7930, 0.0524	1.907
HD 110184	19, 22, 50	0.0210, 0.1781, 0.8008	1.911
HD 110184	01, 02, 22	0.0490, 0.1912, 0.7598	1.917
HD 110184	19, 22, 49	0.0267, 0.2327, 0.7406	1.920
HD 110184	11, 22, 44	0.0211, 0.1572, 0.8218	1.936
HD 110184	02, 22, 49	0.0442, 0.2079, 0.7479	1.937
HD 110184	19, 22, 48	0.0232, 0.2106, 0.7662	1.939
HD 110184	11, 22, 50	0.0182, 0.1179, 0.8639	1.942
HD 110184	22, 27, 44	0.1328, 0.0108, 0.8564	1.950
HD 110184	02, 22, 48	0.0387, 0.1899, 0.7714	1.958
HD 110184	11, 22, 47	0.0148, 0.1158, 0.8695	1.973
HD 110184	19, 22, 44	0.0264, 0.2380, 0.7356	1.981
HD 110184	19, 22, 47	0.0202, 0.1846, 0.7952	1.988
HD 88609	11, 34, 46	0.0016, 0.7382, 0.2602	1.922
HD 88609	18, 34, 46	0.0016, 0.7127, 0.2858	2.038

Notes. The relative contributions F_i and the $\chi^2_{\nu,50}$ are also shown. All of them are accepted fits.

ORCID iDs

A. Psaltis https://orcid.org/0000-0003-2197-0797
M. Jacobi https://orcid.org/0000-0001-8168-4579
F. Montes https://orcid.org/0000-0001-9849-5555
A. Arcones https://orcid.org/0000-0002-6995-3032
C. J. Hansen https://orcid.org/0000-0002-7277-7922
H. Schatz https://orcid.org/0000-0003-1674-4859

References

Abbott, B. P., Abbott, R., Abbott, T., et al. 2017, PhRvL, 119, 161101
Amarsi, A. M., Lind, K., Asplund, M., Barklem, P. S., & Collet, R. 2016, MNRAS, 463, 1518
Andrae, R., Schulze-Hartung, T., & Melchior, P. 2010, arXiv:1012.3754
Angus, C., Williams, M., Andreyev, A., et al. 2023, EPJWC, 279, 11003
Aoki, M., Ishimaru, Y., Aoki, W., & Wanajo, S. 2017, ApJ, 837, 8
Aoki, W., Honda, S., Beers, T. C., et al. 2005, ApJ, 632, 611
Arcones, A., & Bliss, J. 2014, JPhG, 41, 044005
Arcones, A., Fröhlich, C., & Martínez-Pinedo, G. 2012, ApJ, 750, 18
Arcones, A., & Montes, F. 2011, ApJ, 731, 5
Arcones, A., & Thielemann, F. K. 2013, JPhG, 40, 013201
Bisterzo, S., Travaglio, C., Gallino, R., Wiescher, M., & Käppeler, F. 2014, ApJ, 787, 10
Bliss, J. 2020, Nuc-Astro/public_data-representativetrajectories_nuclearphysics-uncertainties: Trajectories used in Phys. Rev. C 101, GitHub, https://github.com/nuc-astro/public_data-RepresentativeTrajectories_NuclearPhysicsUncertainties
Bliss, J., Arcones, A., Montes, F., & Pereira, J. 2017, JPhG, 44, 054003
Bliss, J., Arcones, A., Montes, F., & Pereira, J. 2020, PhRvC, 101, 055807
Bliss, J., Witt, M., Arcones, A., Montes, F., & Pereira, J. 2018, ApJ, 855, 135
Bollig, R., Yadav, N., Kresse, D., et al. 2021, ApJ, 915, 28
Bruenn, S. W., Sieverding, A., Lentz, E. J., et al. 2023, ApJ, 947, 35
Burrows, A., Radice, D., Vartanyan, D., et al. 2020, MNRAS, 491, 2715
Burrows, A., & Vartanyan, D. 2021, Natur, 589, 29
Cain, M., Frebel, A., Ji, A. P., et al. 2020, ApJ, 898, 40
Cavallo, L., Cescutti, G., & Matteucci, F. 2021, MNRAS, 503, 1
Collette, A. 2013, Python and HDF5 (Sebastopol, CA: O'Reilly Media, Inc.)
Côté, B., Eichler, M., Arcones, A., et al. 2019, ApJ, 875, 106
Cowan, J. J., Sneden, C., Lawler, J. E., et al. 2021, RvMP, 93, 015002
Crameri, F. 2021, Scientific color maps, v7.0.1, Zenodo, doi:10.5281/zenodo.5501399
Cristallo, S., Abia, C., Straniero, O., & Piersanti, L. 2015, ApJ, 801, 53
Cyburt, R. H., Amthor, A. M., Ferguson, R., et al. 2010, ApJS, 189, 240
Drout, M., Piro, A., Shappee, B., et al. 2017, Sci, 358, 1570
Eichler, M., Nakamura, K., Takiwaki, T., et al. 2018, JPhG, 45, 014001
Fallis, J., Clark, J. A., Sharma, K. S., et al. 2011, PhRvC, 84, 045807
Fields, B. D., & Wallner, A. 2023, ARNPS, 73, 365
François, P., Depagne, E., Hill, V., et al. 2007, A&A, 476, 935
Fröhlich, C., Hauser, P., Liebendörfer, M., et al. 2006, ApJ, 637, 415
Fröhlich, C., Martínez-Pinedo, G., Liebendörfer, M., et al. 2006, PhRvL, 96, 142502
Goriely, S. 1999, A&A, 342, 881
Hansen, C., Montes, F., & Arcones, A. 2014, ApJ, 797, 123
Hansen, C. J., Andersen, A. C., & Christlieb, N. 2014, A&A, 568, A47
Hansen, C. J., Primas, F., Hartman, H., et al. 2012, A&A, 545, A31
Harris, C. R., Millman, K. J., van der Walt, S. J., et al. 2020, Natur, 585, 357
Harris, J. A., Hix, W. R., Chertkow, M. A., et al. 2017, ApJ, 843, 2
Hill, V., Plez, B., Cayrel, R., et al. 2002, A&A, 387, 560
Hoffman, R., Woosley, S., & Qian, Y.-Z. 1997, ApJ, 482, 951
Honda, S., Aoki, W., Ishimaru, Y., & Wanajo, S. 2007, ApJ, 666, 1189
Horowitz, C. J., Arcones, A., Cote, B., et al. 2019, JPhG, 46, 083001
Hunter, J. D. 2007, CSE, 9, 90
Janka, H.-T., Melson, T., & Summa, A. 2016, ARNPS, 66, 341
Kiss, G. G., Szegedi, T. N., Mohr, P., et al. 2021, ApJ, 908, 202
Kluyver, T., Ragan-Kelley, B., Pérez, F., et al. 2016, in Positioning and Power in Academic Publishing: Players, Agents and Agendas, ed. F. Loizides & B. Schmidt (Amsterdam: IOS Press), 90
Kobayashi, C., Mandel, I., Belczynski, K., et al. 2023, ApJL, 943, L12
Lentz, E. J., Bruenn, S. W., Hix, W. R., et al. 2015, ApJL, 807, L31
Liu, N., Nittler, L. R., Alexander, C. M. O. D., & Wang, J. 2018, SciA, 4, eaao1054
Lodders, K., Palme, H., & Gail, H.-P. 2009, Solar System (Berlin: Springer), 712
Mashonkina, L., Christlieb, N., Barklem, P. S., et al. 2010, A&A, 516, A46
Mohr, P., Fülöp, Z., Gyürky, G., et al. 2021, ADNDT, 142, 101453
Montes, F., Beers, T. C., Cowan, J., et al. 2007, ApJ, 671, 1685
Müller, B., Melson, T., Heger, A., & Janka, H.-T. 2017, MNRAS, 472, 491
Navó, G., Reichert, M., Obergaulinger, M., & Arcones, A. 2023, ApJ, 951, 112
Nishimura, N., Rauscher, T., Hirschi, R., et al. 2019, MNRAS, 489, 1379
Nishimura, N., Sawai, H., Takiwaki, T., Yamada, S., & Thielemann, F.-K. 2017, ApJL, 836, L21
O'Connor, E. 2015, ApJS, 219, 24
Otsuki, K., Honda, S., Aoki, W., Kajino, T., & Mathews, G. J. 2006, ApJL, 641, L117
Otsuki, K., Tagoshi, H., Kajino, T., & Wanajo, S.-y. 2000, ApJ, 533, 424
The pandas development team 2020, pandas-dev/pandas: Pandas, latest, Zenodo, doi:10.5281/zenodo.3509134
Pedregosa, F., Varoquaux, G., Gramfort, A., et al. 2011, JMLR, 12, 2825
Pérez, F., & Granger, B. E. 2007, CSE, 9, 21
Pignatari, M., Wiescher, M., Timmes, F. X., et al. 2013, ApJL, 767, L22
Prantzos, N., Abia, C., Cristallo, S., Limongi, M., & Chieffi, A. 2020, MNRAS, 491, 1832
Pruet, J., Hoffman, R. D., Woosley, S. E., Janka, H. -T., & Buras, R. 2006, ApJ, 644, 1028
Psaltis, A., Arcones, A., Montes, F., et al. 2022, ApJ, 935, 27
Psaltis, A., Chen, A. A., Longland, R., et al. 2022a, PhRvC, 106, 045805
Psaltis, A., Chen, A. A., Longland, R., et al. 2022b, PhRvL, 129, 162701
Qian, Y. Z., & Wasserburg, G. J. 2000, PhR, 333, 77
Qian, Y. Z., & Wasserburg, G. J. 2007, PhR, 442, 237
Qian, Y.-Z., & Woosley, S. 1996, ApJ, 471, 331
Randhawa, J. S., Kanungo, R., Refsgaard, J., et al. 2021, PhRvC, 104, L042801
Rauscher, T., Dauphas, N., Dillmann, I., et al. 2013, RPPh, 76, 066201
Reichert, M., Obergaulinger, M., Aloy, M. Á, et al. 2023a, MNRAS, 518, 1557
Reichert, M., Obergaulinger, M., Eichler, M., Aloy, M. Á, & Arcones, A. 2021, MNRAS, 501, 5733
Reichert, M., Winteler, C., Korobkin, O., et al. 2023b, ApJS, 268, 66
Roederer, I. U., Lawler, J. E., Den Hartog, E. A., et al. 2022, ApJS, 260, 27
Roederer, I. U., Preston, G. W., Thompson, I. B., et al. 2014, AJ, 147, 136
Sakari, C. M., Placco, V. M., Hansen, T., et al. 2018, ApJL, 854, L20
Sandoval, M. A., Hix, W. R., Messer, O. E. B., Lentz, E. J., & Harris, J. A. 2021, ApJ, 921, 113
Scholz, F. W., & Stephens, M. A. 1987, J. Am. Stat. Assoc., 82, 918
Sieverding, A., Kresse, D., & Janka, H.-T. 2023, ApJL, 957, L25
Sneden, C., Cowan, J. J., & Gallino, R. 2008, ARA&A, 46, 241
Sneden, C., Cowan, J. J., Ivans, I. I., et al. 2000, ApJL, 533, L139
Szegedi, T. N., Kiss, G. G., Mohr, P., et al. 2021, PhRvC, 104, 035804
Truran, J. W., Cowan, J. J., Pilachowski, C. A., & Sneden, C. 2002, PASP, 114, 1293

Vartanyan, D., Burrows, A., Radice, D., Skinner, M. A., & Dolence, J. 2019, MNRAS, 482, 351
Wallner, A., Froehlich, M. B., Hotchkis, M. A. C., et al. 2021, Sci, 372, 742
Wanajo, S. 2006, ApJ, 647, 1323
Wanajo, S. 2013, ApJL, 770, L22
Wanajo, S., Janka, H.-T., & Kubono, S. 2011, ApJ, 729, 46
Wanajo, S., Kajino, T., Mathews, G. J., & Otsuki, K. 2001, ApJ, 554, 578
Wanajo, S., Müller, B., Janka, H.-T., & Heger, A. 2018, ApJ, 852, 40
Wang, X., Clark, A. M., Ellis, J., et al. 2023, ApJ, 948, 113
Wasserburg, G. J., Busso, M., & Gallino, R. 1996, ApJL, 466, L109
Wehmeyer, B., López, A. Y., Côté, B., et al. 2023, ApJ, 944, 121
Winteler, C., Käppeli, R., Perego, A., et al. 2012, ApJL, 750, L22
Witti, J., Janka, H.-T., & Takahashi, K. 1994, A&A, 286, 841
Woosley, S., & Hoffman, R. D. 1992, ApJ, 395, 202
Xing, Y. M., Li, K. A., Zhang, Y. H., et al. 2018, PhLB, 781, 358